



Cite this: *Nanoscale*, 2017, **9**, 1645

Tunable electrical properties of multilayer HfSe₂ field effect transistors by oxygen plasma treatment†

Moonshik Kang,^{a,b} Servin Rathi,^a Inyeal Lee,^a Lijun Li,^a Muhammad Atif Khan,^a Dongsuk Lim,^a Yoontae Lee,^a Jinwoo Park,^a Sun Jin Yun,^c Doo-Hyeb Youn,^c Chungsam Jun^b and Gil-Ho Kim^{*a}

HfSe₂ field effect transistors are systematically studied in order to selectively tune their electrical properties by optimizing layer thickness and oxygen plasma treatment. The optimized plasma-treated HfSe₂ field effect transistors showed a high on/off ratio improvement of four orders of magnitude, from 27 to 10⁵, a field effect mobility increase from 2.16 to 3.04 cm² V⁻¹ s⁻¹, a subthreshold swing improvement from 30.6 to 4.8 V dec⁻¹, and a positive threshold voltage shift between depletion mode and enhancement mode, from -7.02 to 11.5 V. The plasma-treated HfSe₂ photodetector also demonstrates a reasonable photoresponsivity from the visible to the near-infrared region of light.

Received 28th October 2016,
Accepted 16th December 2016

DOI: 10.1039/c6nr08467b

www.rsc.org/nanoscale

Introduction

Over the past several years, the discovery of new two-dimensional (2D) materials other than graphene has resulted in enormous interest in research on the basic properties of these materials and their applications in the fields of electronics and optoelectronics.^{1–5} In particular, the family of transition-metal dichalcogenides (TMDs), such as MoS₂ and WSe₂, has shown interesting electrical and optoelectrical characteristics depending upon their phases, *i.e.*, 1T or 2H.^{6–9} Furthermore, the physical properties of these 2D materials can be modulated or improved by stacking different atomically thin layers with different material characteristics.^{10–12} In addition to providing an excellent platform to study the aspects of exotic physics like excitons and Coulomb drag, such TMD heterostructures have huge potential applications in numerous devices like vertical tunneling-based field effect transistors (FETs), atomically thin diodes, light emitting diodes, and solar cells.^{6,13,14} Particularly interesting type II or III band alignments have been predicted in group IVB/VIB-based TMD

heterostructures (*e.g.*, HfSe₂/WSe₂ or HfS₂/MoTe₂), allowing the realization of 2D vertical staggered or broken gap tunnel FETs.^{15,16} In this scheme, the smaller band gap or the high work function of Hf-based TMDs make them suitable for such applications.^{16,17}

Recently, molecular beam epitaxial growth of HfSe₂/MoS₂ (/MoSe₂), and electrical and optoelectrical characterization of hafnium sulfide (HfS₂) have been published by several groups.^{17–22} However, to the best of our knowledge, there have not been many experimental studies on hafnium diselenide (HfSe₂) FETs.^{23,24} Therefore, the properties of HfSe₂-based devices require further research, much like other TMD materials which are in the initial stages of exploration. In particular, passivation-based studies are critical to device performance, especially for novel 2D materials like black phosphorus and Hf-based TMDs which are inherently unstable and prone to degradation under atmospheric conditions.^{22–26}

In this study, we report a simple and efficient approach where a few top layers of HfSe₂ were transformed into hafnium oxide (HfO_x) *via* oxygen (O₂) plasma treatment. This facile process can be used to control the active channel thickness of HfSe₂ FETs and the resulting top oxidized layers can be effective to reduce the ambient induced oxidation of the HfSe₂ layers. We found from our study that the electrical properties of HfSe₂ FETs can be selectively tuned by adjusting the O₂ plasma treatment time. The plasma-treated devices showed an improvement in the on/off ratio (>10⁵) by up to four orders of magnitude and subthreshold swing (30.6 → 4.8 V dec⁻¹) without any significant loss of the field effect mobility (2.16 → 3.04 cm² V⁻¹ s⁻¹). Furthermore, a positive threshold voltage

^aCollege of Information and Communication Engineering and Sungkyunkwan Advanced Institute of Nanotechnology (SAINT), Sungkyunkwan University, Suwon 16419, Republic of Korea. E-mail: ghkim@skku.edu

^bManufacturing Engineering Team, Memory Division, Samsung Electronics Co., Hwasung 18448, Republic of Korea

^cICT Components and Materials Technology Research Division, Electronics and Telecommunications Research Institute, Daejeon 34129, Republic of Korea

†Electronic supplementary information (ESI) available. See DOI: 10.1039/c6nr08467b

shift from depletion mode to enhancement mode ($-7.02 \rightarrow 11.5$ V) was also observed. We also evaluated the performance of HfSe₂ photodetectors for different wavelengths from the visible to the near-infrared region, which showed a maximum photoresponsivity of 2.64×10^4 mA W⁻¹.

Results and discussion

The electrical and optoelectrical properties of these 2D material-based devices strongly depend on their channel thickness. In thinner layers, interfacial scattering is dominant, thus affecting the mobility, while in thicker layers, interlayer resistance becomes a dominant factor leading to the degradation of the mobility.¹⁹ Therefore, before studying the effect of plasma treatment on the device characteristics, we carried out detailed experiments to evaluate the effect of channel thickness on the properties of HfSe₂ FETs. Fig. 1a shows a schematic diagram of HfSe₂ FET with electrical connections (see Methods section for details). To optimize the thickness of HfSe₂, back-gated FETs with channel thicknesses ranging from 4.4 to 79.2 nm were fabricated and measured.

Fig. 1b shows the thickness-dependent Raman spectra of the HfSe₂ flakes. The thicknesses of the flakes were 4.5, 11, and 26 nm, respectively, as measured by atomic force microscopy (AFM) (see the Methods section for details). The two most prominent modes of the Raman spectrum of a few-layered HfSe₂ sample are E_g at 146 cm⁻¹ and A_{1g} at 199 cm⁻¹, which are attributed to in plane and out of plane modes.^{17,27} As can be seen from the Raman spectra, for thinner flakes (~ 4.5 nm) an additional E_g peak appears at 146 cm⁻¹ which fades away as the thickness is increased and disappears when

the flake thickness reaching 11 nm. Similarly, the intensity of the A_{1g} peak increases as the flake thickness decreases.²⁸

In addition to optical characterization, thickness-dependent electrical characteristics were also studied. Fig. 1c shows the transfer characteristics and Fig. 1d shows the plots of the field effect mobility (μ_{FE}) and the on/off ratios ($I_{on/off}$) of HfSe₂ FETs with different flake thicknesses. It can be seen from the figure that the devices with thinner channels showed higher $I_{on/off}$, however, the μ_{FE} deteriorates as interfacial scattering becomes dominant. In contrast, for devices with thicker channels, μ_{FE} maintains larger than average values but $I_{on/off}$ decreases due to screening effects from the bottom layers which result in incomplete depletion of the top layers.²⁹ This inefficient gate control in thicker channels leads to the formation of a parallel conduction path in the top layers, even at off-gate voltages, thus resulting in higher off-currents. The variation of μ_{FE} with the thickness, as seen in Fig. 1d, can be explained by the interplay of interfacial scattering and interlayer resistance in the devices, where the former dominates thinner channels while the latter dominates thicker ones. Therefore, it can be inferred from the results that the optimum channel thickness for the best electrical performance of HfSe₂ FETs lies in the range of ~ 10 to 20 nm. It may be noted that this optimization considered both $I_{on/off}$ and mobility simultaneously to draw conclusion regarding the optimum thickness.

Fig. 2a shows a schematic diagram of the process of treating the channels of HfSe₂ FETs with an O₂ plasma (see the Methods section for details). Before the O₂ plasma treatment, the dimensions of the channel (length, width, and thickness of the channel are 8.2 μ m, 3.6 μ m, and 21.3 nm, respectively) in the HfSe₂ FETs were opened selectively using a standard

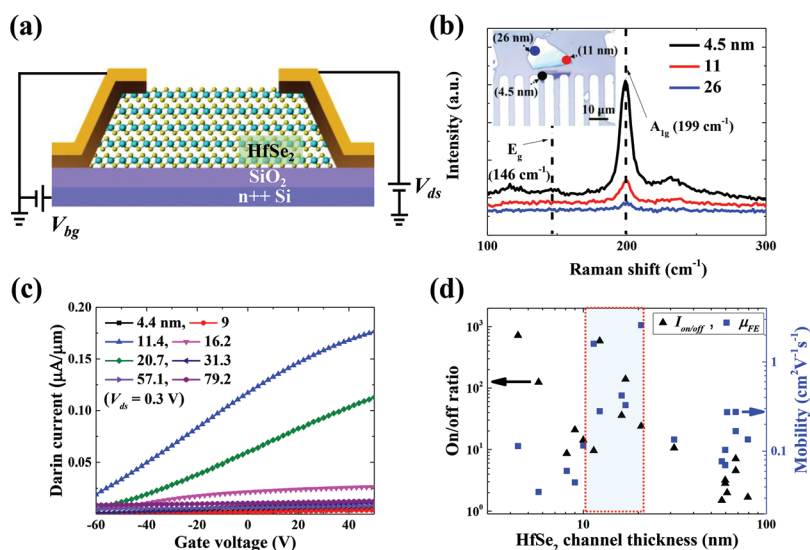


Fig. 1 (a) Schematic diagram of HfSe₂ FET with electrical connections. (b) Thickness-dependent Raman spectra of the HfSe₂ flakes. The thicknesses of the flakes were 4.5, 11, and 26 nm, respectively, as measured by atomic force microscopy (AFM). (c) Transfer characteristics ($I_{ds}-V_{bg}$) of HfSe₂ FETs with different flake thicknesses. (d) The field effect mobility (μ_{FE}) and on/off ratios ($I_{on/off}$) of all devices, showing strong dependence on flake thickness. The optimum thickness of HfSe₂ FETs for the best device performance lies in the range of ~ 10 to 20 nm.

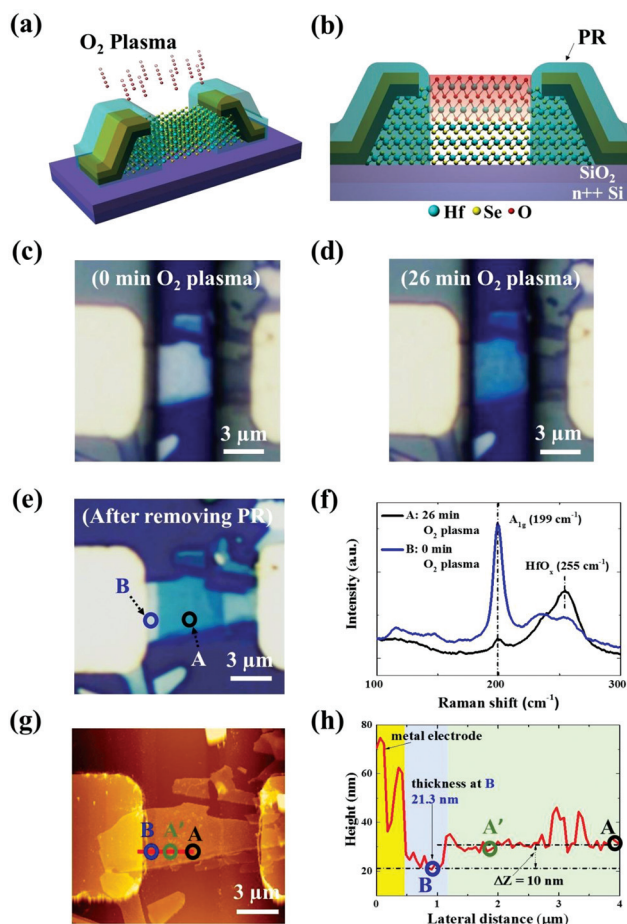


Fig. 2 (a) Schematic diagram of O_2 plasma treatment process applied to the channels of $HfSe_2$ FETs. Before the O_2 plasma treatment, the channel area of $HfSe_2$ FETs was opened selectively using a standard photolithography process. (b) Schematic diagram of top oxidized layers after O_2 plasma treatment of the $HfSe_2$ FETs. During the exposure to O_2 plasma, energetic plasma molecules interact with $HfSe_2$ to form insulating HfO_x layers. Optical images of the $HfSe_2$ FET (c) before, (d) after 26 min of O_2 plasma treatment, and (e) after removing PR in acetone. (f) Raman spectra of O_2 plasma-treated and non-treated areas of the $HfSe_2$ FET. (g) AFM image and (h) line-profile along the red line on the O_2 plasma-treated $HfSe_2$ FET. The average increase in the thickness of the O_2 plasma-treated $HfSe_2$ is approximately 10 nm.

photolithography process (see the ESI for details, Fig. S1†). Fig. 2b shows a schematic diagram of the top oxidized layers after O_2 plasma treatment of the $HfSe_2$ FETs. During the exposure to the O_2 plasma, energetic plasma molecules interact with $HfSe_2$ to form insulating HfO_x layers and their thickness increases with plasma exposure time. This transformation of the top layers into an oxide layer results in the thinning of the active $HfSe_2$ channel, which can be utilized to improve the device characteristics of the electronic FETs. Fig. 2c and d show the optical images of $HfSe_2$ FETs before and after 26 min of O_2 plasma treatment, respectively. Fig. 2e shows the plasma-treated sample after removal of the photoresist (PR). After O_2 plasma treatment, the color contrast between the plasma-treated and non-treated channels indicates a variation in

either the channel thickness or chemical composition. AFM and Raman spectroscopy methods were used to confirm the origin of this variation.

Fig. 2f shows the Raman spectra of the O_2 plasma-treated and non-treated areas of $HfSe_2$ FETs. After O_2 plasma treatment, a new HfO_x Raman peak ($\sim 255\text{ cm}^{-1}$) appears.^{30,31} While the $HfSe_2$ A_{1g} peak position is not changed, the intensity decreases significantly after 26 min of O_2 plasma exposure (see the ESI for details, Fig. S2†). Fig. 2g and h show AFM images and line-profile along the red line of the O_2 plasma-treated $HfSe_2$ FETs, respectively. As seen in the figures, the O_2 plasma treatment results in an increase in the $HfSe_2$ channel thickness, which is consistent with the previously reported results for HfS_2 and WS_2 .^{22,32} This increase in the thickness can be attributed to the expanded interlayer distance due to oxidation²² and the average increase in the thickness is found to be approximately 10 nm (see the ESI for details, Fig. S3†).

X-ray photoelectron spectroscopy (XPS) characterization was carried out to study the modifications of chemical bonding and the formation of additional bonds in pristine and plasma-treated samples (see the Methods section for details). Fig. 3a and c show the XPS spectra of Hf 4f of pristine and plasma-treated $HfSe_2$ samples, respectively. The Hf 4f spectrum from Hf–Se bonding in Fig. 3a consists of two peaks that are attributed to the Hf 4f_{5/2} ($\sim 17.82\text{ eV}$) and 4f_{7/2} ($\sim 16.15\text{ eV}$) levels in $HfSe_2$.^{17,33} The Hf 4f spectrum assigned to the Hf– O_x chemical bonding state in Fig. 3c also consists of two peaks, Hf 4f_{5/2} ($\sim 18.68\text{ eV}$) and 4f_{7/2} ($\sim 17.11\text{ eV}$), which are consistent with the peak positions of HfO_x .^{17,34,35}

Fig. 3b and d show the XPS spectra of the Se 3d levels of pristine and plasma-treated $HfSe_2$ samples, respectively. We detected only one chemical state in the Se 3d spectrum from the pristine $HfSe_2$ samples shown in Fig. 3b, which is assigned to Se–Hf bonding. This peak is composed of two sub-peaks which are attributed to the Se 3d_{3/2} ($\sim 54.47\text{ eV}$) and 3d_{5/2} ($\sim 53.58\text{ eV}$) levels in $HfSe_2$.^{17,36} However, the Se 3d spectrum of the plasma-treated $HfSe_2$ samples, as shown in Fig. 3d, is composed of two chemical states, Se– O_x and Se–Se bonding. Using the deconvolution technique, the best fit was obtained by resolving the spectrum into four Gaussian peaks, where the Se 3d_{3/2} ($\sim 59.95\text{ eV}$) and 3d_{5/2} ($\sim 58.96\text{ eV}$) levels originated from SeO_x , and Se 3d_{3/2} ($\sim 55.97\text{ eV}$) and 3d_{5/2} ($\sim 54.96\text{ eV}$) levels from Se, respectively.^{17,36,37} The absence of Hf–Se bonding in the O_2 plasma-treated samples and the occurrence of additional peaks representing SeO_x and Se clearly indicates the conversion of the top layers of $HfSe_2$ into HfO_x , which leaves other residual materials including SeO_x and Se. Furthermore, the relative intensity of the Se 3d peaks decreased after the plasma treatment, indicating a reduced concentration of Se (Se/Hf ratio reduced from the near ideal of 2.09 to 1.19), which can be attributed to the breaking of Hf–Se bonds and partial desorption of the volatile phase like SeO_x from the surface *via* O_2 plasma treatment.^{25,38}

After detailed chemical analysis, the effect of O_2 plasma treatment on the electrical properties of the $HfSe_2$ FETs was studied (see the Methods section for details). Fig. 4a shows the

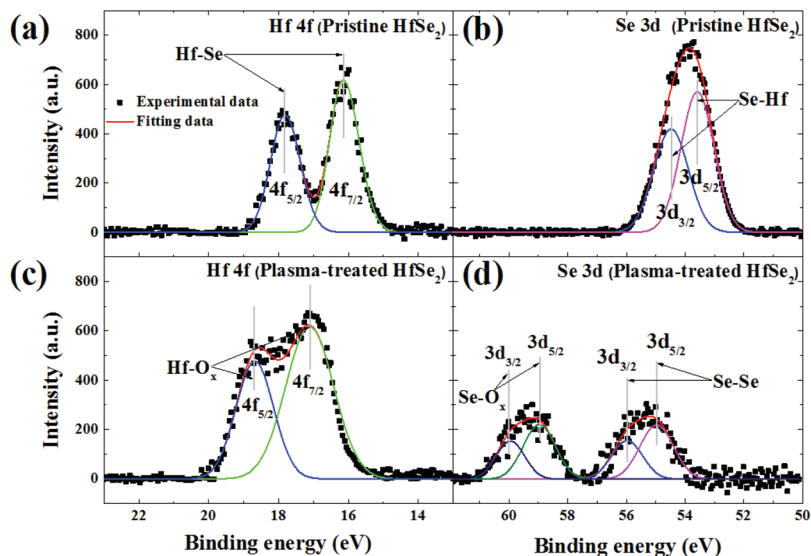


Fig. 3 XPS spectra of (a) Hf 4f and (b) Se 3d levels for the pristine HfSe₂ sample. XPS spectra of (c) Hf 4f and (d) Se 3d levels for the O₂ plasma-treated HfSe₂ sample. The top layers of HfSe₂ are fully converted to HfO_x by exposure to O₂ plasma treatment.

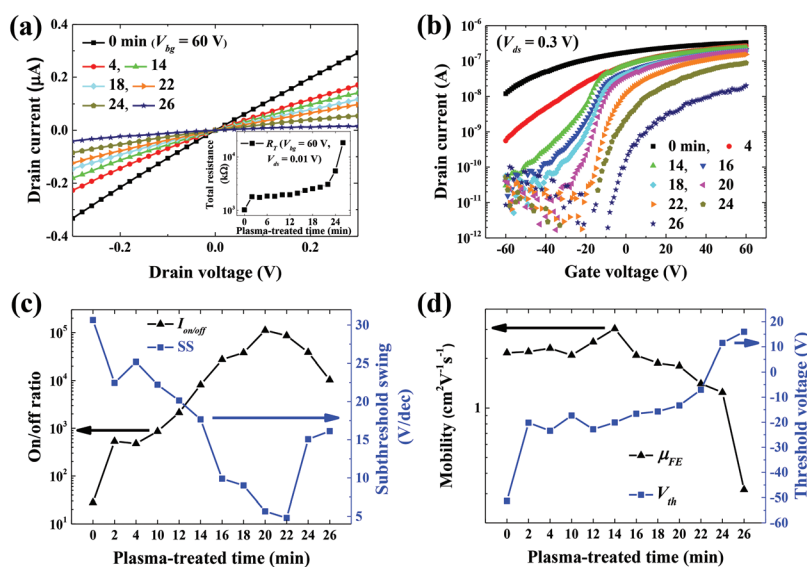


Fig. 4 (a) Output characteristics (I_{ds} - V_{ds}) for HfSe₂ FETs after different O₂ plasma exposure times. The inset shows the total resistance (R_T) of the HfSe₂ FETs as a function of plasma exposure time. (b) Transfer characteristics (I_{ds} - V_{bg}) at $V_{ds} = 0.3$ V for HfSe₂ FETs with different O₂ plasma exposure times, in the semi-log scale. (c) On/off ratio ($I_{on/off}$) and the subthreshold swing (SS) as a function of O₂ plasma treatment time. (d) Field effect mobility (μ_{FE}), and threshold voltage (V_{th}) as a function of O₂ plasma treatment time.

output characteristics of HfSe₂ FETs after O₂ plasma treatment with different exposure times. The linear I_{ds} - V_{ds} curves show good Ohmic behavior for various plasma treatment times. The inset shows the total resistance (R_T) of the HfSe₂ FETs as a function of plasma exposure time. After the first 2 min of O₂ plasma exposure, R_T increases by 75 percent (%). However, with further exposure, R_T is well controlled with just a 5.6% increase every 2 min until 22 min. Fig. 4b shows the transfer characteristics at $V_{ds} = 0.3$ V for HfSe₂ FETs with different O₂ plasma exposure times. Qualitatively, it can be seen from the figure that O₂

plasma treatment results in a positive threshold voltage (V_{th}) shift, higher $I_{on/off}$ and improvements in the subthreshold swing (SS) of the device. Further, for an accurate analysis, the μ_{FE} , $I_{on/off}$, SS, and V_{th} of the device after each plasma exposure are calculated from the I_{ds} - V_{bg} curves. Fig. 4c shows $I_{on/off}$ and SS as a function of O₂ plasma treatment time. $I_{on/off}$ increases from 27 to 1.1×10^5 and SS improves from 30.6 to 4.8 V dec⁻¹ for 20 and 22 min of O₂ plasma treatment, respectively. Fig. 4d shows μ_{FE} and V_{th} as a function of O₂ plasma treatment time, where μ_{FE} increases from 2.16 to 3.04 cm² V⁻¹ s⁻¹ after 14 min

of O₂ plasma treatment. While this variation in μ_{FE} is moderate, but the wide variation in V_{th} can be used to efficiently tune the operation of HfSe₂ FETs from depletion mode ($V_{th} = -7.02$ V, 22 min of O₂ plasma treatment) to enhancement mode ($V_{th} = 11.5$ V, 24 min of O₂ plasma treatment). This indicates that the electrical properties of multilayer HfSe₂ FETs can be tuned efficiently *via* O₂ plasma treatment.

The origin of these variations in device characteristics can be explained by the formation of Hf-based oxide layers, which is evident from both Raman and XPS analyses. During the O₂ plasma treatment, the top layers are oxidized to form HfO_x which results in a reduction of the active channel thickness. As in thick channel devices, the gate electric field at the top layers is screened off by the active channel layers near the SiO₂ interface which results in an ineffective gate control. This consequently leads to both a high off-current and a high negative gate voltage to turn off the device. Therefore, as the top layers are transformed to HfO_x by plasma treatment, the effective channel thickness reduces, thus decreasing the off-current and shifting the V_{th} to positive values (see the ESI for details, Fig. S4 and S5†). This is also quite evident from Fig. 4b and c, where steady shifts in the V_{th} and improvement in the off-current due to better gate control and channel thinning are observed during the successive exposures of the channel to the O₂ plasma. Therefore, important device metrics like $I_{on/off}$ and SS show gradual improvement until an optimum exposure to plasma treatment is reached. Another consequence of O₂ plasma treatment is a reduction in the electron density due to the oxygen doping effect, as the reactive oxygen at the surface can co-exist in different forms such as O²⁻ and O⁻. Since these

moieties are highly electronegative, they can capture free electrons, thus reducing the electron carrier density in the channel (see the ESI for details, Fig. S6 and S7†).³⁹

The V_{th} shifts observed in the plasma-treated devices can also be explained by carrier depletion in the channel as less gate voltage is now required to turn off the channel. Further, an apparent improvement in μ_{FE} can be explained from the interplay of the reduced carrier density and channel thinning *via* plasma treatment, which results in reduced inter-carrier scattering and enhanced confinement of the carrier in the channel. The observed improvement in SS results from better $I_{on/off}$ and gate control over the thinner channel. As seen from the figures, after reaching an optimum state, the key device characteristics start degrading with further plasma treatment. This may be due to excessive oxidation of the top layers, which after reaching the optimum value starts affecting the active channel layers through increased interfacial carrier scattering and the enhanced doping effects of the oxygen-based compounds in the top oxide layers. This is also evident from the V_{th} shift from depletion mode to enhancement mode and a steep fall in μ_{FE} beyond 24 min of O₂ plasma treatment. This decrease in the mobility also affirm that the untreated HfO_x contains defects and the conventional improvements due to high-*k* dielectric are limited in the present case. Further, it was found that as compared to the untreated devices, the top oxidized layers in the O₂ plasma-treated device are more effective to suppress the ambient induced oxidation of the underlying HfSe₂ layers (see the ESI for details, Fig. S8†).

In the next step, we carried out optoelectrical characterization of the plasma-treated HfSe₂ photodetectors. To the best

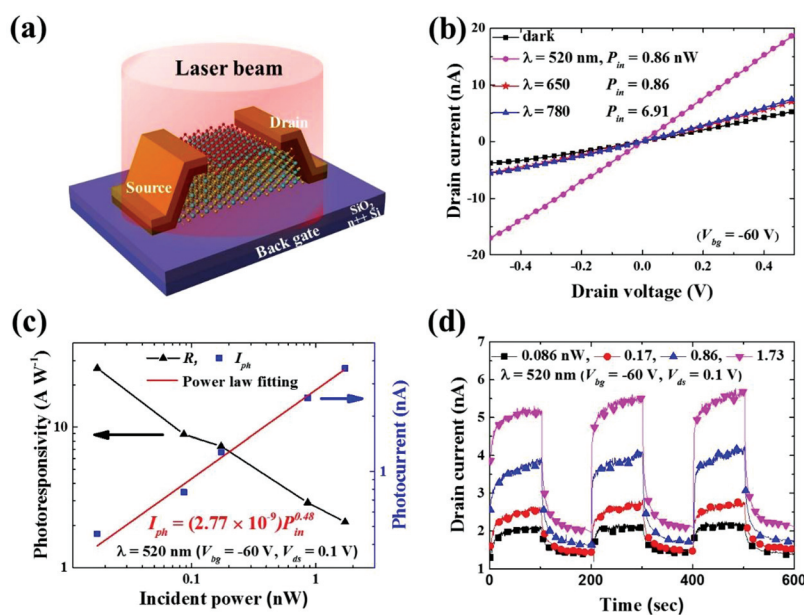


Fig. 5 (a) Schematic diagram of HfSe₂ photodetector under illumination. (b) Output characteristics (I_{ds} - V_{ds}) of HfSe₂ photodetectors in the dark and laser-illumination at wavelengths (λ) of 520, 650, and 780 nm. (c) The photoresponsivity (R) and photocurrent (I_{ph}) of HfSe₂ photodetectors as a function of the effective incident power (P_{in}) at $V_{ds} = 0.1$ V, $V_{bg} = -60$ V, and $\lambda = 520$ nm. The red line represents the fitting curve. (d) The reproducible on/off switching of the HfSe₂ photodetectors with various effective incident powers at $V_{ds} = 0.1$ V, $V_{bg} = -60$ V, and $\lambda = 520$ nm.

of our knowledge, this is the first optoelectrical measurement study on HfSe₂. Fig. 5a shows a schematic diagram of the HfSe₂ photodetector under illumination. Fig. 5b shows the output characteristics of the 21.5 nm thick, 7 min O₂ plasma-treated HfSe₂ photodetector in the dark and laser-illumination at wavelengths (λ) of 520, 650, and 780 nm, where the effective incident power (P_{in}) was 0.86 nW at $\lambda = 520$ and 650 nm, and 6.91 nW at $\lambda = 780$ nm (see the Methods section for details and the ESI for the photoresponse of the pristine HfSe₂ device, Fig. S9†). As seen from the figure, the photodetector recorded its maximum photocurrent (I_{ph}) at $\lambda = 520$ nm, and responded to a broadband of incident wavelengths from the visible ($\lambda = 520$ nm) to the near-infrared region ($\lambda = 780$ nm) of light. The maximum photoresponsivity (R) and specific detectivity (D^*) of the HfSe₂ photodetectors at $\lambda = 520$ nm were calculated as 2.94 A W⁻¹ and 4.65×10^{10} Jones, respectively (see the ESI for details, Fig. S10†). These results are comparable to those of previously reported TMD-based photodetectors.^{40,41} R can be expressed as

$$R = I_{\text{ph}}/(P_{\text{in}}) = (I_{\text{laser}} - I_{\text{dark}})/(P_{\text{in}})$$

where I_{laser} is the device current under illumination and I_{dark} is the dark current.^{40,41} Fig. 5c shows the R and I_{ph} of the HfSe₂ photodetectors as a function of the P_{in} at $V_{\text{ds}} = 0.1$ V, $V_{\text{bg}} = -60$ V, and $\lambda = 520$ nm. As the P_{in} increases from 0.017 to 1.73 nW, R decreases from 26.44 to 2.11 A W⁻¹. This decrease in R with P_{in} may be due to the existence of trap states in or at the interface between the materials. Further, the graph of I_{ph} versus P_{in} can be fitted using the power law relationship:

$$I_{\text{ph}} = (2.77 \times 10^{-9}) P_{\text{in}}^{0.48}$$

The fitted curve was shown with a red line that indicates a near-square root dependence of I_{ph} on P_{in} . This result is due to the finite density of deep donor levels compared with the flux of incident photons.⁴² The non-unity exponent may also be attributed to a complex process of electron-hole generation, trapping, and recombination within HfSe₂.⁴³

Fig. 5d shows the on/off switching of the HfSe₂ photodetectors with various P_{in} at $V_{\text{ds}} = 0.1$ V, $V_{\text{bg}} = -60$ V, and $\lambda = 520$ nm. The HfSe₂ photodetector shows reproducible switching behavior but a relatively long rise (τ_{r} : ~10 s) and decay (τ_{d} : ~20 s) time, respectively.⁴⁴ These rise and decay time were calculated as being between 10% and 90% of increasing and decreasing I_{ph} .

Conclusions

In conclusion, we presented a simple and efficient method of using O₂ plasma treatment to tune the electrical properties of multilayer HfSe₂ FETs. A clear positive threshold voltage shift was observed in the device, from depletion mode to enhancement mode, with the on/off ratio increasing by up to four orders of magnitude. A substantial improvement in the sub-threshold swing was observed without any significant loss of

mobility by adjusting the O₂ plasma exposure time. These improvements were attributed to the formation of insulating HfO_x top layers *via* O₂ plasma treatment and thinning of the channel. Moreover, we demonstrated a strong dependence of HfSe₂ electrical properties on the channel thickness of the device. The thinner channel along with the decrease in the electron density by electronegative oxygen moieties results in an efficient gate control which leads to improved device performances. Optical and chemical characterization by means of Raman spectroscopy, XPS, and AFM measurement confirmed the formation of HfO_x layers after plasma treatment. The optoelectrical measurements of the O₂ plasma-treated HfSe₂ photodetectors demonstrated a reasonable photoresponsivity from the visible to the near-infrared region of light. Our study suggests that the plasma treatment method can be developed into a promising technology to tune the key parameters of TMD devices for various applications, and multilayer HfSe₂ can be used as one of the main materials for electrical and optoelectrical TMD heterostructures in the near future.

Methods

Fabrication of HfSe₂ FETs

The HfSe₂ flakes were produced from commercial bulk HfSe₂ purchased from HQ graphene, *via* standard mechanical exfoliation using the scotch tape technique. HfSe₂ flakes were exfoliated onto a 285 nm thick SiO₂ layer on a heavily doped n-type Si substrate. The back-gated FETs were fabricated *via* photolithography to define the source and drain electrodes and then Cr (10 nm)/Au (30 nm) layers were deposited in an electron beam evaporation system. This was followed by a standard lift-off process in acetone.

Oxygen plasma treatment process

The O₂ plasma treatment process was applied to the HfSe₂ devices using a commercial (COVANCE, Femto Science Inc.) plasma chamber operating at 50 kHz at a power of 50 W, which is the minimum power required to initiate plasma in the chamber. During the O₂ plasma treatment process, the chamber pressure was maintained at ~500 mTorr and O₂ gas flowed at a constant rate of 20 sccm.

AFM, Raman, and XPS characterization

The thickness of HfSe₂ was measured using an AFM (SPA400, SII) in tapping mode under ambient conditions. The Raman spectra of the as-exfoliated and O₂ plasma-treated HfSe₂ were taken at room-temperature under ambient conditions using a WiTech confocal Raman microscope (Alpha300RA, Witec Inc.) with an Nd:YAG laser at a wavelength of 532 nm. The chemical configurations of HfSe₂ were determined *via* X-ray photoelectron spectroscopy (ESCA2000, VG Microtech Inc.) with an Al K α X-ray source ($h\nu = 1486.6$ eV) at a base pressure of $\sim 10^{-10}$ Torr. For XPS measurement, as-exfoliated and 26 min O₂ plasma-treated HfSe₂ samples were prepared on SiO₂ substrates.

Electrical measurement with and without laser illumination

The HfSe₂ FETs and photodetectors were electrically characterized using a Keithley 4200 semiconductor characterization system (4200-SCS, Keithley Inc.) under ambient and under dark conditions. μ_{FE} was extracted using the equation $\mu_{\text{FE}} = (L/W) \times (g_{\text{m}}/C_{\text{ox}}V_{\text{ds}})$, where L is the channel length, W is the channel width, g_{m} is the transconductance which is determined by the slope of the $I_{\text{ds}}-V_{\text{bg}}$ curve, and C_{ox} is the dielectric capacitance between the channel and the back gate per unit area. Dielectric capacitance was calculated using $C_{\text{ox}} = \epsilon_0\epsilon_r/d$, in which ϵ_r is the relative permittivity of SiO₂, ϵ_0 is the free-space permittivity and d is the SiO₂ thickness. For optoelectrical measurement of the photodetector, light sources of different wavelengths ($\lambda = 520, 650, \text{ and } 780 \text{ nm}$) were illuminated with an effective incident power ranging from 0.017 to 6.91 nW.

Acknowledgements

This research was supported by the Basic Science Research Program through the National Research Foundation of Korea (NRF) funded by the Ministry of Education, Science and Technology (No. 2013R1A2A2A01069023) and the Korea Research Fellowship Program through the NRF funded by the Ministry of Science, ICT and Future Planning (NRF-2015H1D3A1062519). This work was partly supported by the Institute for Information & Communications Technology Promotion (IITP) grant funded by the Korea government (MSIP) (B0117-16-1003, Fundamental technologies of two-dimensional materials and devices for the platform of new-functional smart devices).

References

- 1 S. Z. Butler, S. M. Hollen, L. Cao, Y. Cui, J. A. Gupta, H. R. Gutiérrez, T. F. Heinz, S. S. Hong, J. Huang, A. F. Ismach, E. Johnston-Halperin, M. Kuno, V. V. Plashnitsa, R. D. Robinson, R. S. Ruoff, S. Salahuddin, J. Shan, L. Shi, M. G. Spencer, M. Terrones, W. Windl and J. E. Goldberger, *ACS Nano*, 2013, **7**, 2898–2926.
- 2 D. Akinwande, N. Petrone and J. Hone, *Nat. Commun.*, 2014, **5**, 5678.
- 3 G. Fiori, F. Bonaccorso, G. Lannaccone, T. Palacios, D. Neumaier, A. Seabaugh, S. K. Banerjee and L. Colombo, *Nat. Nanotechnol.*, 2014, **9**, 768–779.
- 4 F. Xia, H. Wang, D. Xiao, M. Dubey and A. Ramasubramaniam, *Nat. Photonics*, 2014, **8**, 899–907.
- 5 G. R. Bhimanapati, Z. Lin, V. Meunier, Y. Jung, J. Cha, S. Das, D. Xiao, Y. Son, M. S. Strano, V. R. Cooper, L. Liang, S. G. Louie, E. Ringe, W. Zhou, S. S. Kim, R. R. Naik, B. G. Sumpter, H. Terrones, F. Xia, Y. Wang, J. Zhu, D. Akinwande, N. Alem, J. A. Schuller, R. E. Schaak, M. Terrones and J. A. Robinson, *ACS Nano*, 2015, **9**, 11509–11539.
- 6 D. Jariwala, V. K. Sangwan, L. J. Lauhon, T. J. Marks and M. C. Hersam, *ACS Nano*, 2014, **8**, 1102–1120.
- 7 R. Ganatra and Q. Zhang, *ACS Nano*, 2014, **8**, 4074–4099.
- 8 L. Li, I. Lee, D. Lim, M. Kang, G.-H. Kim, N. Aoki, Y. Ochiai, K. Watanabe and T. Taniguchi, *Nanotechnology*, 2015, **26**, 295702.
- 9 O. Lopez-Sanchez, D. Lembke, M. Kayci, A. Radenovic and A. Kis, *Nat. Nanotechnol.*, 2013, **8**, 497–501.
- 10 A. K. Geim and I. V. Grigorieva, *Nature*, 2013, **499**, 419–425.
- 11 X. Hong, J. Kim, S.-F. Shi, Y. Zhang, C. Jin, Y. Sun, S. Tongay, J. Wu, Y. Zhang and F. Wang, *Nat. Nanotechnol.*, 2014, **9**, 682–686.
- 12 S. Rathi, I. Lee, D. Lim, J. Wang, Y. Ochiai, N. Aoki, K. Watanabe, T. Taniguchi, G.-H. Lee, Y.-J. Yu, P. Kim and G.-H. Kim, *Nano Lett.*, 2015, **15**, 5017–5024.
- 13 T. Roy, M. Tosun, X. Cao, H. Fang, D.-H. Lien, P. Zhao, Y.-Z. Chen, Y.-L. Chueh, J. Guo and A. Javey, *ACS Nano*, 2015, **9**, 2071–2079.
- 14 C.-H. Lee, G.-H. Lee, A. M. van der Zande, W. Chen, Y. Li, M. Han, X. Cui, G. Arefe, C. Nuckolls, T. F. Heinz, J. Guo, J. Hone and P. Kim, *Nat. Nanotechnol.*, 2014, **9**, 676–681.
- 15 V. O. Özçelik, J. G. Azadani, C. Yang, S. J. Koester and T. Low, *Phys. Rev. B: Condens. Matter*, 2016, **94**, 035125.
- 16 C. Gong, H. Zhang, W. Wang, L. Colombo, R. M. Wallace and K. Cho, *Appl. Phys. Lett.*, 2013, **103**, 053513.
- 17 R. Yue, A. T. Barton, H. Zhu, A. Azcatl, L. F. Pena, J. Wang, X. Peng, N. Lu, L. Cheng, R. Addou, S. McDonnell, L. Colombo, J. W. P. Hsu, J. Kim, M. J. Kim, R. M. Wallace and C. L. Hinkle, *ACS Nano*, 2015, **9**, 474–480.
- 18 K. E. Aretouli, P. Tsipas, D. Tsoutsou, J. Marquez-Velasco, E. Xenogiannopoulou, S. A. Giamini, E. Vassalou, N. Kelaidis and A. Dimoulas, *Appl. Phys. Lett.*, 2015, **106**, 143105.
- 19 K. Xu, Z. Wang, F. Wang, Y. Huang, F. Wang, L. Yin, C. Jiang and J. He, *Adv. Mater.*, 2015, **27**, 7881–7887.
- 20 T. Kanazawa, T. Amemiya, A. Ishikawa, V. Upadhyaya, K. Tsuruta, T. Tanaka and Y. Miyamoto, *Sci. Rep.*, 2016, **6**, 22277.
- 21 K. Xu, Y. Huang, B. Chen, Y. Xia, W. Lei, Z. Wang, Q. Wang, F. Wang, L. Yin and J. He, *Small*, 2016, **12**, 3106–3111.
- 22 S. H. Chae, Y. Jin, T. S. Kim, D. S. Chung, H. Na, H. Nam, H. Kim, D. J. Perello, H. Y. Jeong, T. H. Ly and Y. H. Lee, *ACS Nano*, 2016, **10**, 1309–1316.
- 23 M. Kang, S. Rathi, I. Lee, D. Lim, J. Wang, L. Li, M. A. Khan and G.-H. Kim, *Appl. Phys. Lett.*, 2015, **106**, 143108.
- 24 M. J. Mleczko, C. Zhang, H. R. Lee, H.-H. Kuo, B. Magyari-Köpe, Z.-X. Shen, R. G. Moore, I. R. Fisher, Y. Nishi and E. Pop, in *Device Research Conference (DRC), 2016 74th Annual*, 2016, pp. 1–2.
- 25 G. Mirabelli, C. McGeough, M. Schmidt, E. K. McCarthy, S. Monaghan, I. M. Povey, M. McCarthy, F. Gity, R. Nagle, G. Hughes, A. Cafolla, P. K. Hurley and R. Duffy, *J. Appl. Phys.*, 2016, **120**, 125102.
- 26 J. Pei, X. Gai, J. Yang, X. Wang, Z. Yu, D.-Y. Choi, B. Luther-Davies and Y. Lu, *Nat. Commun.*, 2016, **7**, 10450.

- 27 X. Zhang, Q.-H. Tan, J.-B. Wu, W. Shi and P.-H. Tan, *Nanoscale*, 2016, **8**, 6435–6450.
- 28 H. Li, Q. Zhang, C. C. R. Yap, B. K. Tay, T. H. T. Edwin, A. Olivier and D. Baillargeat, *Adv. Funct. Mater.*, 2012, **22**, 1385–1390.
- 29 S. Das and J. Appenzeller, *Nano Lett.*, 2013, **13**, 3396–3402.
- 30 P. E. Quintard, P. Barbéris, A. P. Mirgorodsky and T. Merle-Méjean, *J. Am. Ceram. Soc.*, 2002, **85**, 1745–1749.
- 31 S. N. Tkachev, M. H. Manghnani, A. Niilisk, J. Aarik and H. Mändar, *J. Mater. Sci.*, 2005, **40**, 4293–4298.
- 32 M. Yamamoto, S. Dutta, S. Aikawa, S. Nakaharai, K. Wakabayashi, M. S. Fuhrer, K. Ueno and K. Tsukagoshi, *Nano Lett.*, 2015, **15**, 2067–2073.
- 33 T. Ito, M. Iwami and A. Hiraki, *J. Phys. Soc. Jpn.*, 1981, **50**, 1978–1985.
- 34 S. J. Wang, P. C. Lim, A. C. H. Huan, C. L. Liu, J. W. Chai, S. Y. Chow, J. S. Pan, Q. Li and C. K. Ong, *Appl. Phys. Lett.*, 2003, **82**, 2047–2049.
- 35 V. A. Gritsenko, T. V. Perevalov and D. R. Islamov, *Phys. Rep.*, 2016, **613**, 1–20.
- 36 M. Shenasa, S. Sainkar and D. Lichtman, *J. Electron Spectrosc. Relat. Phenom.*, 1986, **40**, 329–337.
- 37 E. New, I. Hancox, L. A. Rochford, M. Walker, C. A. Dearden, C. F. McConville and T. S. Jones, *J. Mater. Chem. A*, 2014, **2**, 19201–19207.
- 38 A. Azcatl, S. KC, X. Peng, N. Lu, S. McDonnell, X. Qin, F. de Dios, R. Addou, J. Kim, M. J. Kim, K. Cho and R. M. Wallace, *2D Mater.*, 2015, **2**, 014004.
- 39 J. Jiang and S. Dhar, *Phys. Chem. Chem. Phys.*, 2016, **18**, 685–689.
- 40 L. Zeng, L. Tao, C. Tang, B. Zhou, H. Long, Y. Chai, S. P. Lau and Y. H. Tsang, *Sci. Rep.*, 2016, **6**, 20343.
- 41 W. Choi, M. Y. Cho, A. Konar, J. H. Lee, G.-B. Cha, S. C. Hong, S. Kim, J. Kim, D. Jena, J. Joo and S. Kim, *Adv. Mater.*, 2012, **24**, 5832–5836.
- 42 Z. Fan, P.-C. Chang, J. G. Lu, E. C. Walter, R. M. Penner, C.-H. Lin and H. P. Lee, *Appl. Phys. Lett.*, 2004, **85**, 6128–6130.
- 43 H. Kind, H. Yan, B. Messer, M. Law and P. Yang, *Adv. Mater.*, 2002, **14**, 158–160.
- 44 M. Buscema, J. O. Island, D. J. Groenendijk, S. I. Blanter, G. A. Steele, H. S. J. van der Zant and A. Castellanos-Gomez, *Chem. Soc. Rev.*, 2015, **44**, 3691–3718.